Draft version October 2, 2018
Typeset using LaTeX **twocolumn** style in AASTeX62

Magnetic field tomography in two clouds towards Ursa Major using HI fibers

Aris Tritsis,[1] Christoph Federrath,[1] and Vasiliki Pavlidou[2,3]

[1] *Research School of Astronomy and Astrophysics, Australian National University, Canberra, ACT 2611, Australia*
[2] *Department of Physics and Institute for Theoretical and C omputational Physics, University of Crete, 70013, Heraklion, Greece*
[3] *Foundation for Research and Technology Hellas, IESL & Institute of Astrophysics, Voutes, 70013, Heraklion, Greece*

ABSTRACT

The diffuse, atomic interstellar medium is observed to be full of thin, linear structures, usually referred to as "fibers". Fibers exhibit similar properties to linear structures found in molecular clouds, termed striations. Suggestive of a similar formation mechanism, both striations and fibers appear to be ordered, well-aligned with the magnetic field and exhibit quasi-periodicity. The prevailing formation mechanism for striations involves the excitation of fast magnetosonic waves. Based on the theory of fast magnetosonic waves, and through a combination of velocity centroids and column density maps, Tritsis et al. (2018) developed a method for estimating the plane-of-sky (POS) magnetic field from molecular cloud striations. Here we apply this method in two HI clouds with fibers along the same line-of-sight (LOS) towards the ultra-high-energy cosmic-ray hotspot, at the boundaries of Ursa Major. For the cloud located closer to Earth, where Zeeman observations from the literature were also available, we find general agreement in the distributions of the LOS and POS components of the magnetic field. We find relatively large values for the total magnetic field (ranging from $\sim$10 to $\sim$20 μG) and an average projection angle with respect to the LOS of $\sim 50^{\circ}$. For the cloud located further away, we also find a large value for the POS component of the magnetic field of 15^{+8}_{-3} μG. We discuss the potential of our new magnetic-field tomography method for large-scale application. We also consider the implications of our findings in this specific direction on the accuracy of current reconstructions of the Galactic magnetic field and on the propagation of the highest-energy cosmic rays through the interstellar medium.

Keywords: ISM: clouds – ISM: molecules – ISM: magnetic fields – methods: observational

1. INTRODUCTION

Large Galactic HI surveys such as the Galactic Arecibo L-Band Feed Array HI (GALFA-HI) (Peek et al. 2011; Peek et al. 2018), Parkes Galactic All Sky Survey (GASS) (McClure-Griffiths et al. 2009; Kalberla et al. 2010; Kalberla & Haud 2015) and Effelsberg–Bonn HI Survey (EBHIS) (Kerp et al. 2011; Winkel et al. 2016) have revealed the ubiquitous presence of parallel, elongated, quasi-periodic structures in HI clouds. These structures, referred to as "fibers" in the literature, are observed to be well aligned with the plane-of-sky (POS) magnetic field as this is probed by polarization measurements (McClure-Griffiths et al. 2006; Clark et al. 2014; Clark et al. 2015; Planck Collaboration et al. 2016a; Clark 2018; Jelić et al. 2018).

Corresponding author: Aris Tritsis
Aris.Tritsis@anu.edu.au

Fibers bear important similarities to structures found in the outskirts of molecular clouds, dubbed "striations". Striations are low-density, elongated, magnetically-aligned structures (Goldsmith et al. 2008; Miville-Deschênes et al. 2010; Palmeirim et al. 2013; Alves de Oliveira et al. 2014; Cox et al. 2016; Malinen et al. 2016; Panopoulou et al. 2016). Through a series of numerical experiments, Tritsis & Tassis (2016) have demonstrated that the most probable formation mechanism for striations is that of compressible fast magnetosonic waves. In this physical picture, magnetic pressure waves compress the gas creating over-densities that align parallel to the magnetic field. A prediction from this physical model has been recently confirmed through the discovery of normal modes in the striations of the isolated cloud Musca (Tritsis & Tassis 2018). Normal modes in Musca are established due to the trapping of magnetosonic waves by sharp gradients in their

propagation speed between the cloud and the ambient medium.

Magnetic pressure is dominant over thermal and turbulent pressures in regions with fibers (Heiles 1989; Dickey & Lockman 1990). The dimensionless properties (i.e. the plasma β, defined as the ratio of thermal pressure to magnetic pressure, and the Alfvén Mach number) between striations and fibers are approximately the same. Thus, striations and fibers are likely to share the same formation mechanism.

Tritsis et al. (2018) recently developed a method for estimating the strength of the POS magnetic field through a combined analysis of column density and velocity centroid maps of striations. The method can be applied to individual clouds in different velocity slices and can thus be used to tomographically map the POS magnetic field. Zeeman measurements of the line-of-sight (LOS) magnetic field can also be taken in different velocity channels (e.g. Heiles & Troland 2004). Apart from the strength of the LOS magnetic field, Zeeman measurements also yield its direction with the astronomical convention being that positive magnetic fields point away from the observer provided that the Stokes V is computed as the excess of right-circular polarization over the left-circular polarization (for a review on Zeeman observations conventions we refer the reader to Robishaw 2008). Combined, the two measurements can yield the total strength of the magnetic field, its angle with respect to the LOS and its direction in different clouds along a sight-line.

Complete knowledge of the 3D structure of the magnetic field of the Galaxy would be extremely important for studies of the interstellar medium (in the context of interstellar cloud formation and evolution, star formation, and galaxy formation and evolution); but also for cosmic-ray propagation studies (e.g. Orlando & Strong 2013; Planck Collaboration et al. 2016b; Pierre Auger Collaboration et al. 2017a; Magkos & Pavlidou 2018). At the highest energies ($\geqslant 10^{19}$ eV), where cosmic rays despite being deflected by the magnetic field are not completely isotropized, knowledge of the 3D structure of the magnetic field could be used to reconstruct the path of individual cosmic rays through the Galaxy. Thus, by recovering the original velocity direction of cosmic rays before entering the Galaxy, such studies could elucidate the origin of observed cosmic-ray hotspots (Abbasi et al. 2014; Pierre Auger Collaboration et al. 2017b; Abbasi et al. 2018) and provide electromagnetic constraints on cosmic-ray composition, independent of particle physics (Pavlidou & Tomaras 2018). Such a cosmic-ray hotspot is observed towards Ursa Major, making this region ideal for tomographically mapping the magnetic field. At the same time, knowledge of the 3D structure of the magnetic field and dust alignment and emission properties (for a recent review on grain alignment see Andersson et al. 2015) could be used to predict the expected polarization in regions away from the Galactic plane. Such information would be invaluable for cosmic microwave background polarization (CMB) experiments and the complications that arise due to dust foregrounds (BICEP2/Keck Collaboration et al. 2015; Planck Collaboration et al. 2016c; Tassis & Pavlidou 2015).

In this paper, we provide the first estimate of the strength of the POS magnetic field in two clouds along the same sight-line towards the boundaries of Ursa Major with Camelopardalis and Draco. For the cloud located closer to Earth, we combine our results with Zeeman measurements from the literature (Goodman et al. 1994; Myers et al. 1995). To measure the POS component of the magnetic field we apply the method by Tritsis et al. (2018), developed for molecular cloud striations. In §2 we summarize the theoretical background described in detail in Tritsis et al. (2018). The observations we used for our analysis are presented in §3. In §4 we employ these observations to estimate the magnetic field. We discuss our results in §5 and summarize in §6.

2. METHOD

By linearising the continuity equation, the induction equation of ideal magnetohydrodynamics (MHD), and assuming that the displacement of the gas is described by a plane-wave solution (for details see Tritsis et al. 2018) we obtain:

$$\delta \mathbf{v} = -\sum_n i A_n \omega_n e^{i(\mathbf{k_n r}-\omega_n t)} \tag{1}$$

$$\delta N_H = N_H^0 \sum_n A_n k_n i e^{i(\mathbf{k_n r}-\omega_n t)} \tag{2}$$

$$\delta B = B_0 \sum_n A_n k_n i e^{i(\mathbf{k_n r}-\omega_n t)} \tag{3}$$

where ω is the frequency of the waves, A is the amplitude, k is the wavenumber and the subscript n is used to denote different waves. Equation 1 is written in the frame of reference of the cloud such that the perturbation in velocity (δv) in the perpendicular-to-the-magnetic-field direction is measured with respect to the bulk velocity (v_0) of the cloud. In Equation 2, $N_{\rm H}^0$ is the mean column density and $\delta N_{\rm H}$ is the perturbation in column density. Similarly, in Equation 3, B_0 and δB are the mean magnetic field and the perturbation in the magnetic field, such that $B_{tot} = B_0 + \delta B$ and $N_{\rm H}^{\rm tot} = N_{\rm H}^0 + \delta N_{\rm H}$.

In Equations 1, 2 & 3, the exponential part is the same and only the coefficients change. Thus, the spatial

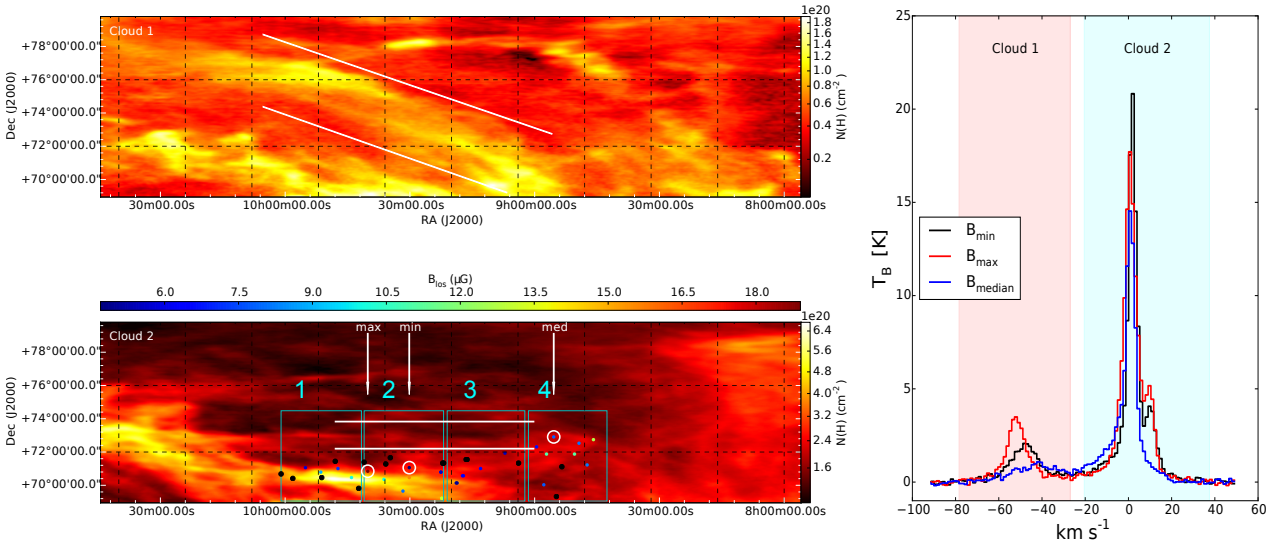

Figure 1. Upper left panel: column density of far cloud (Cloud 1). Lower left panel: column density of near cloud (Cloud 2). On the column density map of Cloud 2 we overplot with colour-coded dots the magnetic field measurement of Myers et al. (1995) from Zeeman measurements. The values of the LOS magnetic field from these measurements are given in the horizontal colorbar. Black points are non-detection Zeeman measurements. All Zeeman measurements yield positive values. White lines show the approximate direction of fibers. White arrows mark the positions where the value of the LOS magnetic field is minimum, maximum and equal to the median value from all measurements. The cyan rectangles annotated with numbers, mark 4 regions where we performed our analysis individually (see text). Right panel: spectral lines where the Zeeman magnetic field measurement is maximum, minimum and equal to the median value of all measurements (marked with white circles in the lower left panel). The pink and cyan regions mark the velocity range we considered for producing the column density of Cloud 1 and Cloud 2, respectively.

power spectra of the observed velocity, column density and magnetic field should peak at the same wavenumbers. Observationally, such power spectra can be computed by considering cuts perpendicular to the long axis of fibers. The power in the column density power spectra $|P_{N_H^1}|^2$ would be $|N_H^0 A_n k_n|^2$ and the power in velocity centroid power spectra $|P_{v_1}|^2$ would be $|\omega_n A_n|^2$. We introduce the parameter Γ, defined in Tritsis et al. (2018) as the square root of the ratio of the power of velocity power spectra over the power of column density power spectra:

$$\Gamma_n = \sqrt{\frac{|P_{v_1}|^2}{|P_{N_H^1}|^2}} = \frac{\omega_n}{k_n}\frac{1}{N_H^0} \tag{4}$$

The term ω_n/k_n in the latter Equation can be substituted from the dispersion relation of fast magnetosonic waves (for a review on MHD waves see Spruit 2013):

$$\frac{\omega_n}{k_n} = \sqrt{\frac{1}{2}\left[(v_A^2 + c_s^2) + \sqrt{(v_A^2 + c_s^2)^2 - 4v_A^2 c_s^2 \cos\phi}\,\right]} \tag{5}$$

where $v_{\rm A}$ is the Alfvén speed (defined as $v_{\rm A} = {\rm B}_0/\sqrt{4\pi\rho_0}$, where ρ_0 is the mean density), $c_{\rm s}$ is the sound speed and ϕ is the angle between the wavevector and the magnetic field such that, when $\phi = \pi/2$, the waves propagating in the medium are magnetic pressure waves exactly perpendicular to the magnetic field. In Equation 5 the sound speed $c_{\rm s}$ can be ignored since ${v_{\rm A}}^2 \gg {\rm c_s}^2$. Additionally, by considering only the waves that propagate perpendicular to the magnetic field, we obtain for the dispersion relation of fast magnetosonic waves that $\omega_n/k_n \approx v_{\rm A}$. Finally, by combining the latter equation with Equation 4, we obtain:

$$\Gamma_n = \frac{v_A}{N_H^0} = \frac{B_0}{\sqrt{4\pi\rho_0}}\frac{1}{N_H^0} \Rightarrow B_0 = \Gamma_n N_H^0 \sqrt{4\pi\rho_0}. \tag{6}$$

For a full description of the simplifications made and a thorough justification of the assumptions entering this derivation, we refer the reader to Tritsis et al. (2018). Equation 6 is valid when the magnetic field lies entirely on the POS and the LOS component is zero. When the magnetic field lies at an angle θ with respect to the POS, the *intrinsic* perturbations (δv) in the velocity component perpendicular to the magnetic field will be *observed* as $\delta v \cos\theta$ and the power in the spectra of velocity centroids perpendicular to fibers will be $|\omega_n A_n \cos\theta|^2$. Thus, by taking projection effects into account, we find:

$$B_0 \cos\theta = B_0^{pos} = \Gamma_n N_H^0 \sqrt{4\pi\rho_0}. \tag{7}$$

Consequently, the method can only probe the POS component of the magnetic field and the angle θ can be found in combination with measurements of the LOS component via Zeeman observations.

3. OBSERVATIONS

For our analysis we use publicly available data from the EBHIS survey (Winkel et al. 2016) and published Zeeman measurements (Goodman et al. 1994; Myers et al. 1995). The spectral resolution of the EBHIS data is 1.29 km s^{-1}, the angular resolution is $\sim$ 11 arcmins and the data are stray-radiation corrected. The analysis of the Zeeman observations by Myers et al. (1995) is consistent with all astronomical conventions.

Along the same sight-line as the Zeeman observations there are two clouds (see right panel of Figure 1). We obtained the column density of each cloud assuming optically thin conditions:

$$N_{\rm H} = 1.823 \times 10^{18} [{\rm cm}^{-2}] \times \int {\rm T_B}\ [1/{\rm K}]\ {\rm dv}\ [{\rm km\ s}^{-1}]^{-1} \tag{8}$$

(Dickey & Lockman 1990; Chengalur et al. 2013) where $T_{\rm B}$ is the brightness temperature and dv is the velocity increment measured in km s^{-1}. Our results are shown in Figure 1. The upper and lower left panels show the column density map of the cloud located further away from Earth (henceforth "Cloud 1") and the cloud located closer to Earth (henceforth "Cloud 2"), respectively. The colour-coded dots overplotted on the lower left panel are the results from the Zeeman observations by Myers et al. (1995). Non-detections are overploted as black dots. In the right panel we plot 3 spectral lines for 3 different lines-of-sight: where the magnetic field from Zeeman measurements is minimum, where it is maximum and where it equals the median value of all measurements. The pink shaded region marks the velocity range of Cloud 1 and the light blue shaded region marks the velocity range of Cloud 2. In order to investigate whether the magnetic field changes direction we separate Cloud 2 in 4 regions shown with the green rectangles in the bottom left panel in Figure 1. We then apply the method by Tritsis et al. (2018) in each of these regions individually and compare our results with the Zeeman measurements from each region.

In order to apply the method by Tritsis et al. (2018) we created the first-moment map of velocity of each cloud by fitting one or two Gaussian distributions to each of the spectral lines of each pixel and computing the velocity of each cloud as a weighted average of the two Gaussians. Then we considered the mean and standard deviation of the first-moment map of each cloud. Cloud 1 is centred at -43 $\pm$ 6 km s^{-1} and Cloud 2 at -0.5 $\pm$ 3.7 km s^{-1}.

4. RESULTS

4.1. *Cloud 1*

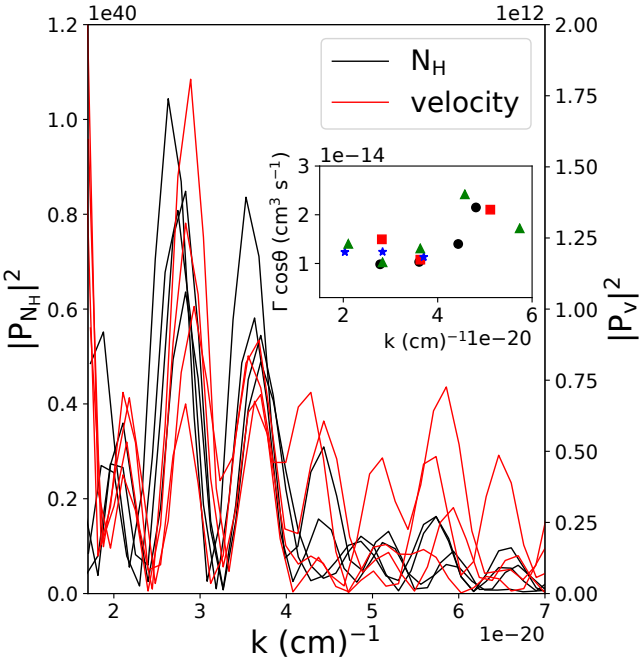

Figure 2. Example of power spectra for Cloud 1 of velocity centroid cuts perpendicular to fibers (red lines) and column density cuts perpendicular to fibers (black lines). The power spectra peak at approximately the same wavenumbers, in agreement with the theoretical predictions of § 2. The inset figure shows the parameter Γ as a function of the wavenumber for each of the power spectra. Different symbols denote our results from each individual set (velocity and column density) of spectra.

We consider cuts perpendicular to fibers in both the column density map and the first-moment map of velocity and compute their power spectra. We then compute the parameter Γ from the powers of the velocity and column density spectra at the peaks. In order to consider a peak in the velocity power spectrum as common with the peak in the column density power spectrum, we require that the distance between their respective wavenumbers is not larger than 15% the value of the wavenumber in column density in the location of the peak. We further apply the criterion that the parameter Γ is only computed from peaks that have powers greater than 10% the maximum power in the power spectrum of each cut. Finally, we require that a power spectrum must have in total more than 2 peaks with power greater that 10% the maximum power. In this manner, we avoid spurious peaks and ensure that failed Gaussian fits from the process of producing the first-moment map do not affect our results.

Examples of column density and velocity power spectra are shown in Figure 2 (black and red lines respectively). In the inset figure we plot the parameter Γ as a function of the wavenumber for each set of peaks that

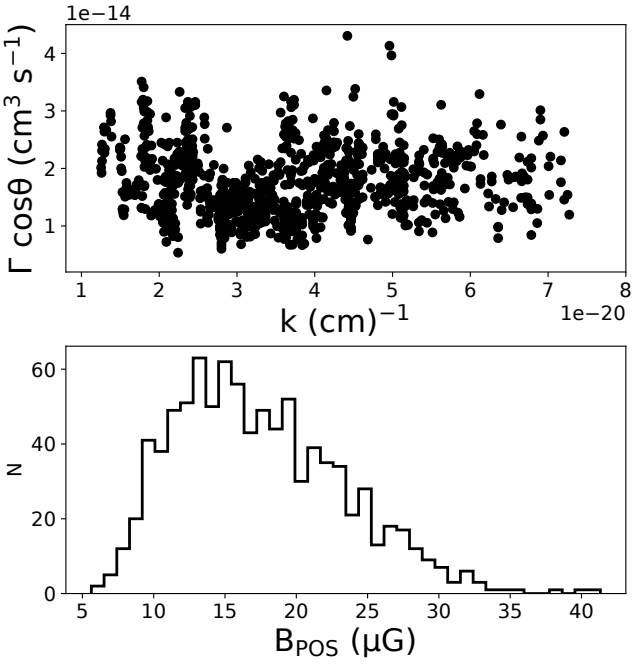

Figure 3. Upper panel: same as the inset of Figure 2 but from all cuts perpendicular to fibers. In agreement with the theoretical predictions of § 2, despite the scatter there is no correlation of the parameter Γ with the wavenumber. Lower panel: distribution of the POS magnetic field values, derived from all the points shown in the upper panel.

fulfil all our criteria from the power spectra shown. The power spectra of velocity and column density have peaks at approximately the same spatial frequencies. The variation of power between different peaks is similar in both the velocity and column density power spectra. For example, in both the velocity and column density power spectra, the second peak has the maximum power, the third peak has the second most power and the first peak has the least power amongst these three peaks. Thus, the results presented in Figure 2 are in agreement with the theoretical predictions from § 2, supporting our original hypothesis, that fibers, similarly to molecular cloud striations, are created from hydromagnetic waves.

In the upper panel of Figure 3 we show the parameter Γ as a function of the wavenumber in each peak. Since the variation of power between different wave-modes follows the same pattern for velocity and column density power spectra (see Figure 2), the ratio of their powers remains approximately constant, in agreement with the theoretical predictions of § 2. The constant ratio of powers as a function of the wavenumber is not an effect of stacking the results from many peaks. This is demonstrated in the inset figure of Figure 2 where we show the parameter Γ as a function of the wavenumber from each individual set of spectra. In the lower panel of Figure 3 we plot the distribution of magnetic field values derived from the values of the parameter Γ shown in the upper panel, the density of the cloud and the mean column density of each respective column density cut. We assume that the number density of the cloud is 10 cm^{-3}. The mode with the 16th and 84th percentiles is 15^{+8}_{-3} μG. Thus, the derived magnetic field value for Cloud 1 is larger than typical values measured in HI clouds and the values derived from models (Heiles 1989; Haverkorn 2015).

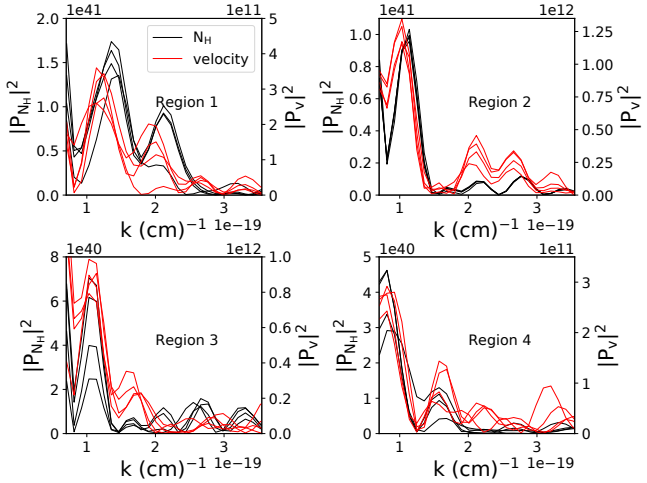

Figure 4. Power spectra of velocity centroid and column density cuts (red and black lines respectively) in the four regions of Cloud 2. As in Cloud 1, the power spectra peak at approximately the same wavenumbers.

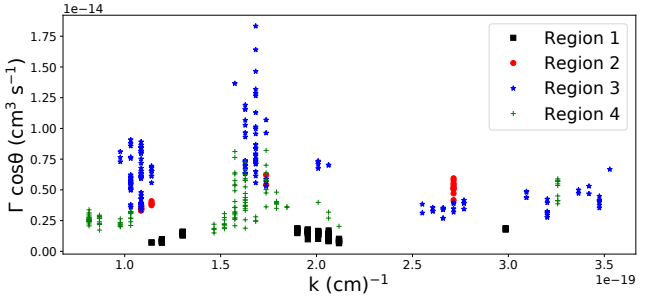

Figure 5. Same as in Figure 3 but for the four regions of Cloud 2.

4.2. *Cloud 2*

We repeat our analysis for Cloud 2 which is located closer to Earth and for which additional Zeeman measurements are available. We separate Cloud 2 into 4 regions (from 1 to 4 as shown in Figure 1). In Figure 4 we show examples of power spectra of velocity and column density cuts from all regions. In agreement with the theoretical analysis of § 2 and the results for Cloud 1 the power spectra peak at approximately the same

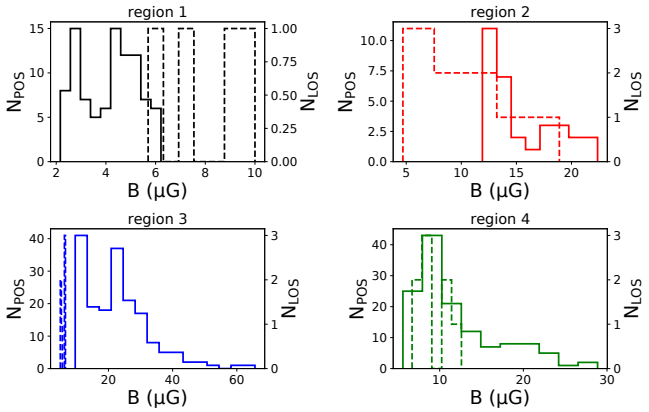

Figure 6. Distributions for the POS magnetic field for each of the four regions of Cloud 2. Especially for region 3, the derived magnetic field values are unusually high. Dashed lines show the distributions of the LOS magnetic field values for each of the four regions measured via Zeeman observations.

wavenumbers and the variations in the power of velocity and column density follow each other well.

In Figure 5 we plot the parameter Γ as a function of the wavenumber for each of the four regions of Cloud 2. Results for region 1 are shown with black squares, for region 2 with red dots, for region 3 with blue stars and for region 4 with green crosses. For each of the four regions the value of the parameters Γ remains approximately constant for different wavenumbers. This is again in agreement with the theoretical considerations of § 2 and the results for Cloud 1.

In Figure 6 we plot the distributions of magnetic field values derived from the points shown in Figure 5 for region 1 (solid black line), region 2 (solid red line), region 3 (solid blue line) and region 4 (solid green line) for Cloud 2. Dashed lines show the LOS components of the magnetic field for the same regions from Zeeman observations by Myers et al. (1995). As in Cloud 1, the POS magnetic field values are computed from Equation 7 where for N_H^0 we use the mean column density of each respective column density cut. From the adopted distance of Cloud 2 (see Appendix A), the mean column density, the size of the region and assuming that the LOS dimension is equal to the size of the region projected on the POS, the number density of Cloud 2 is ~ 10 cm^{-3}. The mode with the 16th and 84th percentiles is 4^{+1}_{-1} μG for region 1, 14^{+7}_{-2} μG for region 2, 17^{+14}_{-4} μG for region 3 and 10^{+8}_{-2} μG for region 4. In reality, the density of Cloud 2 may be much higher (see § 5). Thus, the values quoted above should be interpreted as lower limits.

In Figure 1 there is evidence of a column density gradient moving from region 1 to region 4 and thus region 1 might be denser than region 4. Assuming that the density in region 1 is a factor of two larger than that of region 3 or 4, the mode of the POS magnetic field strength will be 5^{+2}_{-1} μG. Thus, a density gradient from region 1 to region 4 cannot explain the differences seen in the distributions of the magnetic field between different regions. A more plausible explanation is that the magnetic field changes direction between different regions.

In Figure 7 we summarize our results with a 3D view of the clouds inside the Galaxy.

5. DISCUSSION

According to the Monte-Carlo simulations by Chengalur et al. (2013), departures from isothermality do not significantly affect the derived column density which is computed within a factor of 2 of the true value. However, in order to achieve that accuracy, the optical depth has to be known from absorption studies. Even if such studies were available for the two clouds analysed in this paper, knowledge of the LOS dimension is still required in order to better constrain their density (that enters the calculations) from the column density. The mean density of the cold neutral medium is ~ 60 cm^{-3} (Heiles & Troland 2003). Based on the column densities derived for the clouds, a fraction of their mass might also be in the form of molecular hydrogen (Planck Collaboration et al. 2011). Thus, the value of 10 cm^{-3} adopted for the density of the two clouds should be considered as a lower limit. However, the POS component of the magnetic field scales as the square root of density. Thus, despite these uncertainties, the true value of the POS component of the magnetic field in each cloud would not be significantly affected by updated density estimates and would remain within a factor of two higher than the values quoted here.

In Cloud 2 the distributions of the values of the POS and LOS components of the magnetic field are in fair agreement. However, significant variation is observed. In region 1, the LOS component is higher than the POS component ($\sim 24°$ with respect to the LOS) whereas in region 2 the opposite trend is observed with the POS component being higher than the LOS component ($\sim 54°$ with respect to the LOS) and the two distributions overlap. In region 3 the POS component becomes much higher than the LOS component ($\sim 71°$ with respect to the LOS) and with no overlap between the two distributions and finally, in region 4 the two components are approximately the same and equal to ~ 10 μG ($\sim 51°$ with respect to the LOS). Such a behaviour can be potentially explained with the mean magnetic field following an Alfvén wave primarily polarized in the LOS direction. However, more Zeeman measurements are required in order to reach more robust conclusions.

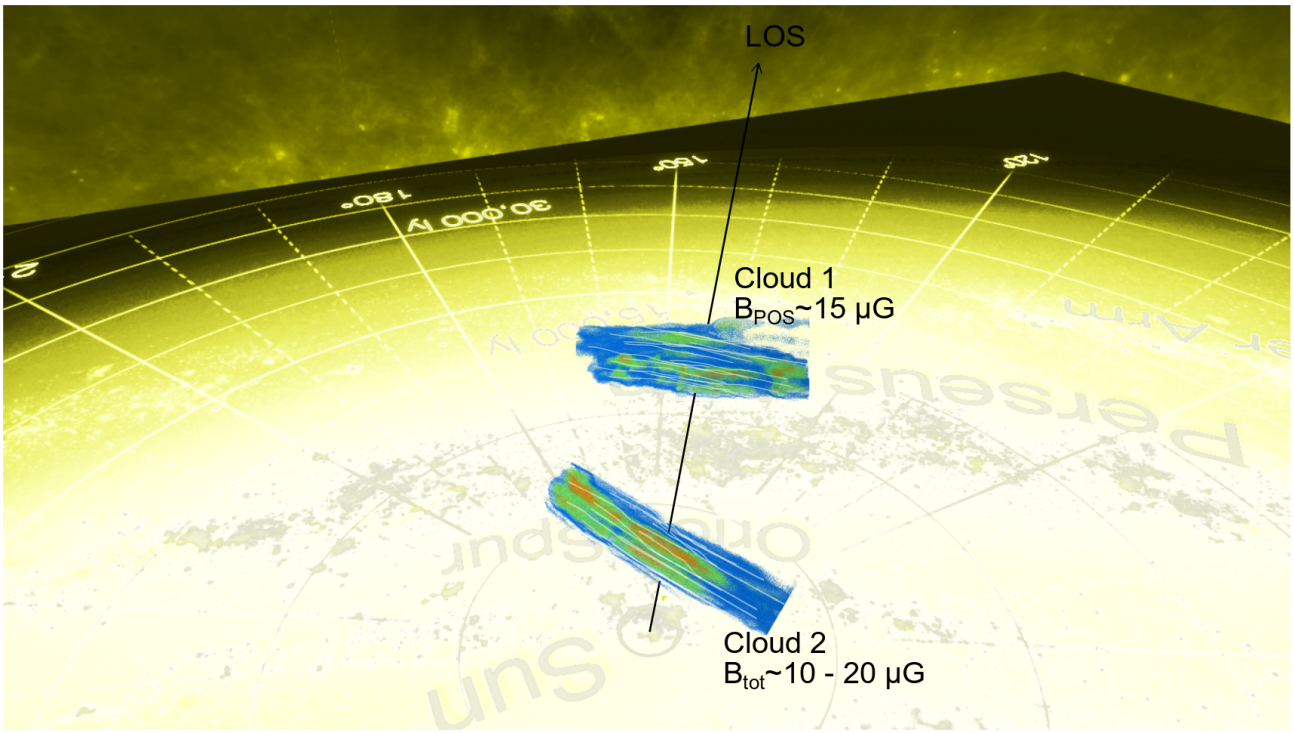

Figure 7. 3D view of the two clouds and their location in the Galaxy. The magnetic field of each cloud is shown with the white lines. The black arrow shows the LOS where the two clouds are observed (produced with the Space Nebula Plugin for Unreal Engine 4).

5.1. *Nature of Fibers*

The upper panel of Figure 3 and Figure 5 represents the dispersion relation of fast magnetosonic waves derived from observations of fibers. Caldwell et al. (2017) analysed Planck polarization data and found that the parameter space required for MHD turbulence to account for observations is very limited. This is further supported by the fact that the ratio of the turbulent to ordered component of the magnetic field is found to be below unity (Planck Collaboration et al. 2016a; Planck Collaboration et al. 2016d; Planck Collaboration et al. 2018). In the case of Burgers turbulence (Burgers 1948), the power in the velocity power spectra scales as $P_v \propto k^{-2}$ (Solomon et al. 1987) and the power in column density power spectra for mildly supersonic clouds without self-gravity scales as $P_{N_H} \propto k^{-1}$ (Federrath & Klessen 2013). Observationally, the velocity spectral index found for HI clouds at high galactic latitudes is ~ 4 and that of column density is ~ 3 (Chepurnov et al. 2010). Thus, in the case of turbulence, the ratio of powers of column density and velocity power spectra, or equivalently the parameter Γ, should depend on the wavenumber as $\Gamma \propto k^{-1}$. This is in contradiction to the results presented in the upper panel of Figure 3 and in Figure 5. However, it is unclear what the dependence of the parameter Γ on the wavenumber would be in the case of turbulence, if the spectral indices were computed only in the direction perpendicular to field lines.

Goodman et al. (1994) presented in graphical form the results from Zeeman measurements by Myers et al.(1995). They found that a profile of IRAS 100 μm flux and a profile of magnetic field measurements followed each other very well. This is in agreement with the theoretical predictions of § 2 in which the column density, velocity centroids and magnetic field variations should all be correlated for a cut across fibers.

5.2. *Implications for the nature and propagation of cosmic rays*

The values we derived for the magnetic field strength using our local, tomographic method are considerably larger than the values predicted by global Galactic magnetic field models that rely on fitting a mix of likely magnetic field components to line-of-sight integrated observables such as Faraday rotations, Synchrotron emission, or polarized dust emission. In particular, Galactic field models (Sun et al. 2008; Jansson & Farrar 2012) estimate a magnetic field 3-5 times weaker than our estimate at the distance of the near cloud (200 pc), and a factor at least 5-8 times weaker than our estimate at the distance of the far cloud (1 kpc). The disagreement is even larger if we instead adopt the (higher) kinematic

distances for the clouds (see Appendix A), or if we adopt a higher value for the volume density.

This result has particularly important implications since the sight-line we have examined is in the general direction of the northern ultra-high-energy cosmic-ray hotspot identified by the Telescope Array Collaboration (Abassi et al. 2014). If these magnetic field values are typical for this general region of the sky, the implication is that the highest-energy cosmic rays ($\gtrsim 6 \times 10^{19}$ eV), among which the hotspot has been identified, get deflected by $\gtrsim 10^{\circ}$ over their propagation through the Galaxy *alone* if they are *protons* (see, e.g., Magkos & Pavlidou 2018). This deflection magnitude is comparable to the radial extent of the excess as estimated by the Telescope Array Collaboration (10°, Abassi et al. 2014). The implication in this case would be that the cosmic rays responsible for the Telescope Array hotspot *have to be protons*, as heavier nuclei would deflect more, proportionally to their atomic number Z, and hence produce a much more extended and less pronounced excess. However, the most recent Auger Collaboration results for the composition of ultra-high-energy cosmic rays (based on the reconstruction of air showers produced in collisions between cosmic rays and atmospheric atoms) detected by the southern-hemisphere, high-statistics cosmic-ray observatory favour a heavier composition, assuming the Standard Model of Particle Physics holds without modifications in ultra-LHC energies, up to 100 TeV. That our results (based only on electromagnetic propagation of cosmic rays in the Galactic field, i.e. physics much more certain to hold up to the highest energies) are not consistent with this finding can be explained in two ways: either the composition of the northern hotspot is different from that produced by the typical cosmic-ray source; or new physics sets in at center-of-mass energies ~ 50 TeV, as has been suggested for other reasons by several authors (e.g., Farrar & Allen 2013; Anchordoqui et al. 2017; The Pierre Auger Collaboration et al. 2017a; Tomar 2017; Pavlidou & Tomaras 2018).

5.3. *Future prospects*

In this paper we tomographically estimated the value of the POS magnetic field of only a very small region of the sky. However, available HI exist for the entire sky and up to very large distances (≤ 600 km s^{-1}) (HI4PI Collaboration et al. 2016). Such data can be processed with the Rolling Hough Transform (Clark et al. 2014) in velocity slices. Such an analysis was already performed for the entire second data release of the GALFA-HI survey, yielding the orientation angle of fibers. With the orientation angle known, the process of considering cuts perpendicular to fibers and applying the method developed by Tritsis et al. (2018) can be fully automated. Advancements in polarization measurements and the upcoming PASIPHAE (Polar-Areas Stellar-Imaging in Polarization High-Accuracy Experiment)[1] optical-polarimetry survey will yield a 3D map of the POS orientation of the Galactic magnetic field. Thus, we aim to apply the method to large fractions of the sky in a follow-up study.

6. SUMMARY

We used the theory of MHD waves and applied the method developed by Tritsis et al. (2018) to derive the POS component of the magnetic field from spectroscopic observations of fibers for two clouds along one line of sight close to Ursa Major. Our results were combined with existing measurements of the LOS magnetic field from Zeeman observations. We find that for both clouds the magnetic field is a factor of ~ 5 larger than what theoretical models of the global Galactic magnetic field predict (Sun et al. 2008; Jansson & Farrar 2012). More specifically, the median value of the magnetic field for the cloud further away from Earth is 15^{+8}_{-3} μG. For the cloud located closer to Earth the POS magnetic field ranges from 4^{+1}_{-1} to 17^{+14}_{-4} μG with the variations in the LOS component of the magnetic field in rough anti-correlation.

The fact that the theoretical predictions from the model developed for striations (Tritsis & Tassis 2016) applies in observations of fibers, strongly suggests that fibers are created from hydromagnetic waves. Finally, our results of the strength of the magnetic field have important implications about the nature of cosmic rays.

ACKNOWLEDGEMENTS

We thank R. Skalidis, G. Panopoulou, K. Tassis, E. Ntormousi and G. Magkos for useful comments and discussions. C. F. acknowledges funding provided by the Australian Research Council (Discovery Projects DP150104329 and DP170100603, and Future Fellowship FT180100495), and the Australia-Germany Joint Research Cooperation Scheme (UA-DAAD). 3D-Visualizations made with Space Nebula Plugin for Unreal Engine 4 (Fabian Fuchs & Linus Fuchs, private communication: Thauros-Development@outlook.com). The data analysis presented in this work used high-performance computing resources provided by the Leibniz Rechenzentrum and the Gauss Centre for Supercomputing (grants pr32lo, pr48pi and GCS Large-scale project 10391), the Partnership for Advanced Computing in Europe (PRACE grant pr89mu), the Australian

[1] http://pasiphae.science/

National Computational Infrastructure (grant ek9), and the Pawsey Supercomputing Centre with funding from the Australian Government and the Government of Western Australia, in the framework of the National Computational Merit Allocation Scheme and the ANU Allocation Scheme.

REFERENCES

Abbasi, R. U., Abe, M., Abu-Zayyad, T., et al. 2014, ApJL, 790, L21

Abbasi, R. U., Abe, M., Abu-Zayyad, T., et al. 2018, arXiv:1802.05003

Alves de Oliveira, C., Schneider, N., Merín, B., et al. 2014, A&A, 568, A98

Anchordoqui, L. A., Goldberg, H., & Weiler, T. J. 2017, PhRvD, 95, 063005

Andersson, B.-G., Lazarian, A., & Vaillancourt, J. E. 2015, ARA&A, 53, 501

BICEP2/Keck Collaboration, Planck Collaboration, Ade, P. A. R., et al. 2015, Physical Review Letters, 114, 101301

Burgers, J.-M. 1948, Advances in Applied Mechanics, 1, 171

Caldwell, R. R., Hirata, C., & Kamionkowski, M. 2017, ApJ, 839, 91

Chepurnov, A., Lazarian, A., Stanimirović, S., Heiles, C., & Peek, J. E. G. 2010, ApJ, 714, 1398

Chambers, K. C., Magnier, E. A., Metcalfe, N., et al. 2016, arXiv:1612.05560

Chengalur, J. N., Kanekar, N., & Roy, N. 2013, MNRAS, 432, 3074

Clark, S. E., Peek, J. E. G., & Putman, M. E. 2014, ApJ, 789, 82

Clark, S. E., Hill, J. C., Peek, J. E. G., Putman, M. E., & Babler, B. L. 2015, Physical Review Letters, 115, 241302

Clark, S. E. 2018, ApJL, 857, L10

Cox, N. L. J., Arzoumanian, D., André, P., et al. 2016, A&A, 590, A110

Dickey, J. M., & Lockman, F. J. 1990, ARA&A, 28, 215

Farrar, G. R., & Allen, J. D. 2013, European Physical Journal Web of Conferences, 53, 07007

Federrath, C., & Klessen, R. S. 2013, ApJ, 763, 51

Goldsmith, P. F., Heyer, M., Narayanan, G., et al. 2008, ApJ, 680, 428-445

Goodman, A. A., Myers, P. C., Gusten, R., & Heiles, C. 1994, The First Symposium on the Infrared Cirrus and Diffuse Interstellar Clouds, 58, 425

Green, G. M., Schlafly, E. F., Finkbeiner, D., et al. 2018, MNRAS, 478, 651

Haverkorn, M. 2015, Magnetic Fields in Diffuse Media, 407, 483

Heiles, C. 1989, ApJ, 336, 808

Heiles, C., & Troland, T. H. 2003, ApJ, 586, 1067

Heiles, C., & Troland, T. H. 2004, ApJS, 151, 271

HI4PI Collaboration, Ben Bekhti, N., Flöer, L., et al. 2016, A&A, 594, A116

Jansson, R., & Farrar, G. R. 2012, ApJL, 761, L11

Jelić, V., Prelogović, D., Haverkorn, M., Remeijn, J., & Klindžić, D. 2018, arXiv:1806.06634

Kalberla, P. M. W., McClure-Griffiths, N. M., Pisano, D. J., et al. 2010, A&A, 521, A17

Kalberla, P. M. W., & Haud, U. 2015, A&A, 578, A78

Kerp, J., Winkel, B., Ben Bekhti, N., Flöer, L., & Kalberla, P. M. W. 2011, Astronomische Nachrichten, 332, 637

King, O. G., Blinov, D., Ramaprakash, A. N., et al. 2014, MNRAS, 442, 1706

Magkos, G., & Pavlidou, V. 2018, arXiv:1802.03409

Malinen, J., Montier, L., Montillaud, J., et al. 2016, MNRAS, 460, 1934

McClure-Griffiths, N. M., Dickey, J. M., Gaensler, B. M., Green, A. J., & Haverkorn, M. 2006, ApJ, 652, 1339

McClure-Griffiths, N. M., Pisano, D. J., Calabretta, M. R., et al. 2009, ApJS, 181, 398

Miville-Deschênes, M.-A., Martin, P. G., Abergel, A., et al. 2010, A&A, 518, L104

Myers, P. C., Goodman, A. A., Gusten, R., & Heiles, C. 1995, ApJ, 442, 177

Orlando, E., & Strong, A. 2013, MNRAS, 436, 2127

Palmeirim, P., André, P., Kirk, J., et al. 2013, A&A, 550, A38

Panopoulou, G. V., Psaradaki, I., & Tassis, K. 2016, MNRAS, 462, 1517

Pavlidou, V., & Tomaras, T. 2018, arXiv:1802.04806

Peek, J. E. G., Heiles, C., Douglas, K. A., et al. 2011, ApJS, 194, 20

Peek, J. E. G., Babler, B. L., Zheng, Y., et al. 2018, ApJS, 234, 2

The Pierre Auger Collaboration, Aab, A., Abreu, P., et al. 2017a, arXiv:1708.06592

Pierre Auger Collaboration, Aab, A., Abreu, P., et al. 2017b, Science, 357, 1266

Planck Collaboration, Abergel, A., Ade, P. A. R., et al. 2011, A&A, 536, A24

Planck Collaboration, Adam, R., Ade, P. A. R., et al. 2016a, A&A, 586, A135

Planck Collaboration, Adam, R., Ade, P. A. R., et al. 2016b, A&A, 596, A103

Planck Collaboration, Adam, R., Ade, P. A. R., et al. 2016c, A&A, 586, A133
Planck Collaboration, Aghanim, N., Alves, M. I. R., et al. 2016d, A&A, 596, A105
Planck Collaboration, Aghanim, N., Akrami, Y., et al. 2018, arXiv:1807.06212
Robishaw, T. 2008, Ph.D. Thesis
Solomon, P. M., Rivolo, A. R., Barrett, J., & Yahil, A. 1987, ApJ, 319, 730
Skrutskie, M. F., Cutri, R. M., Stiening, R., et al. 2006, AJ, 131, 1163
Spruit, H. C. 2013, arXiv:1301.5572
Sun, X. H., Reich, W., Waelkens, A., & Enßlin, T. A. 2008, A&A, 477, 573
Tassis, K., & Pavlidou, V. 2015, MNRAS, 451, L90
Tomar, G. 2017, PhRvD, 95, 095035
Tritsis, A., & Tassis, K. 2016, MNRAS, 462, 3602
Tritsis, A., & Tassis, K. 2018, Science, 360, 635
Tritsis, A., Federrath, C., Schneider, N., & Tassis, K. 2018, submitted
Wenger, T. V., Balser, D. S., Anderson, L. D., & Bania, T. M. 2018, ApJ, 856, 52
Winkel, B., Kerp, J., Flöer, L., et al. 2016, A&A, 585, A41

APPENDIX

A. DISTANCE ESTIMATES

Recently, Wenger et al. (2018) developed a Monte-Carlo code for estimating the kinematic distances to clouds. Using their code and the derived velocity centres of the clouds, we find that the distance to Cloud 1 is 3.64 ± 0.96 kpc and the upper limit for the distance of Cloud 2 is 410 pc. However, kinematic distances are not so robust away from the Galactic disk. Green et al. (2018) provided a 3D map of interstellar dust reddening from Pan-STARRS 1 (Chambers et al. 2016) and 2MASS (Skrutskie et al. 2006) photometric data. Based on their map, in Figure A1 we show the reddening as a function of distance for the coordinates where the two clouds are located. From the points where the reddening curves exhibit an abrupt increase it can be seen that the distance to Cloud 1 appears to be close to $\sim 0.8 - 1$ kpc (i.e. a factor of 3 less than its kinematic distance). The distance to Cloud 2 can be identified at ~ 200 pc. Polarization measurements with the RoboPol instrument (King et al. 2014) at the Skinakas Observatory in Crete also place the first cloud between 200 and 500 pc (R. Skalidis - private communication). These distance estimates are used to crudely estimate the number density of each cloud (see § 4), compare are results to global Galactic magnetic field models and in order to put our results in the greater context of cosmic-ray propagation implications. Here, we adopt a value of 1 kpc for the distance to Cloud 1 and 200 pc for the distance to Cloud 2.

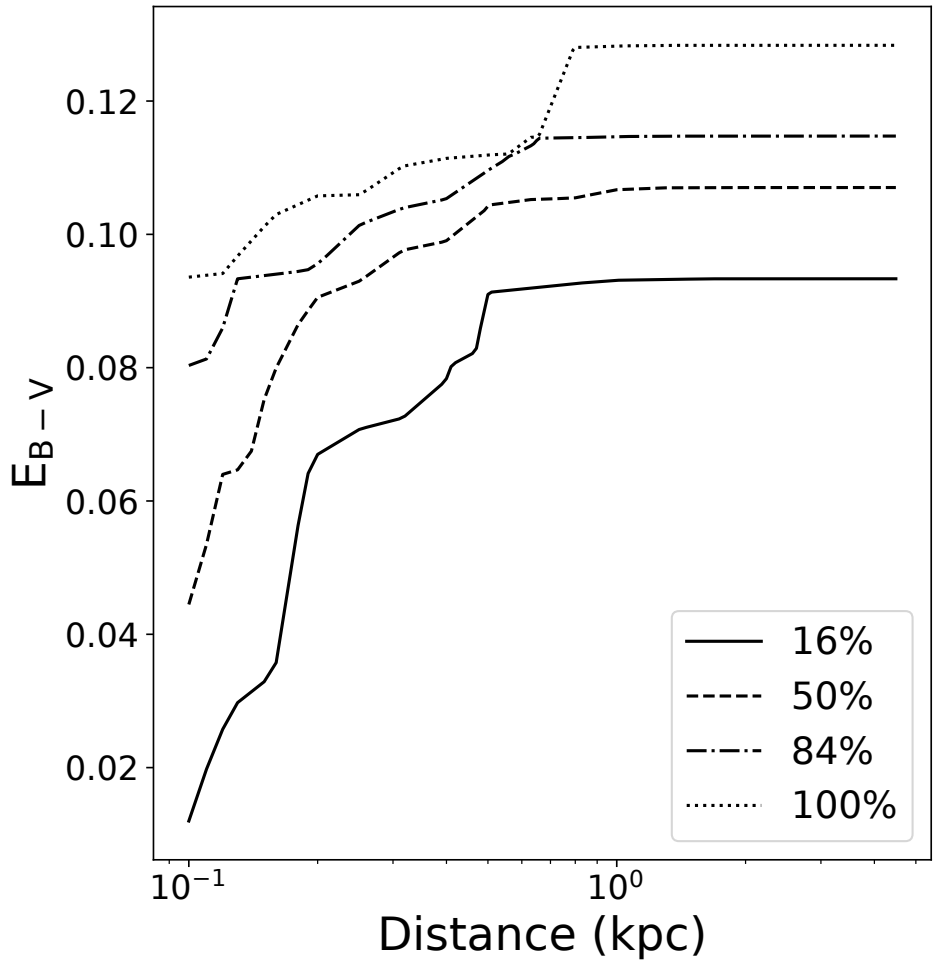

Figure A1. Reddening as a function of distance from the dust reddening map by Green et al. (2018). Different lines represent different percentiles of reddening. The distance to Cloud 1 is estimated to ~ 0.8 - 1 kpc (second sudden rise in reddening), less than computed kinematically and the distance to Cloud 2 is ~ 200 - 500 pc (first sudden rise in reddening).